Bidirectional Anisotropic Reflectance of Snow and Sea Ice in AVHRR Channel 1 and Channel 2 Spectral Regions—Part II: Correction Applied to Imagery of Snow on Sea Ice

Zhonghai Jin and James J. Simpson

Abstract—Advanced Very High Resolution Radiometer (AVHRR) images acquired over the Arctic ocean often show strong bidirectional reflectance of snow on sea ice. The observed anisotropic reflectance characteristics of these images are consistent with the theoretical analysis presented in Part I of this study. The anisotropic reflectance at the top of atmosphere (TOA) is simulated by radiative transfer modeling and the results show a good model–observation agreement. Based on these modeling results, a method was developed to correct the effect of anisotropic reflectance on AVHRR images in channels 1 and 2. Results show the method is effective and efficient. Comparisons of TOA snow reflectance before and after anisotropic correction show that the systematic and large variation of snow reflectance across the scan lines of an image due to satellite viewing/illumination geometry can either be eliminated or greatly reduced by applying the correction algorithm.

Index Terms—Anisotropic reflectance correction, bidirectional reflectance, radiation.

I. INTRODUCTION

S NOW cover on sea ice is one of the major characteristics of the polar oceans. It not only interrupts the energy exchanges between the atmosphere and the ocean, but also highly reflects the solar radiation incident on the ocean surface back to space. Due to the highly-reflective snow/ice, the highly absorptive open oceans, and temporal and spatial variation in their areal extent, the net solar radiation also has great spatial and temporal variation. This makes the polar region a very dynamic climate region.

For climate modeling in the polar region, accurate estimates of the solar energy partition in the atmosphere and ocean are critical. Therefore, accurate assessment of the amount of reflected solar radiation over snow/ice covered ocean is needed [1]–[3]. Although many *in situ* measurements of snow albedo have been made (e.g., [4]–[6]), we have to rely on satellite observations for large-scale, high spatial, and temporal coverage of albedo at the surface and the top of atmosphere (TOA). The Advanced Very High Resolution Radiometer (AVHRR) measurements from the National Oceanic and Atmospheric Administration's (NOAA's), Washington, DC, polar orbiting satellites provide the best data source for deriving albedo, because several passes are collected per day over the polar region. Like all observations from space, however, each AVHRR observation is limited to a certain angular direction for a given pixel. Also, the AVHRR data cover a wide range of view angles across any scan line. Therefore, if the angular dependence of the reflectance of snow is ignored, then the albedo or radiation flux derived from the radiance observed by the AVHRR instrument might have a large error due to the inherent anisotropy of snow reflectance.

Some studies have retrieved snow (and sea ice) albedo from AVHRR data (e.g., [7]–[12]), but the effect of bidirectional reflectance has generally not been considered and/or well corrected. In fact, comparisons of *in situ* and AVHRR-derived albedo over Arctic snow have shown a more favorable agreement when the view geometry effect is considered [8], [11]. Part I of this study analyzed the anisotropic reflectance of snow and sea ice in AVHRR channels 1 and 2 using a radiative transfer model specifically developed for the polar atmosphere, snow/ice, and ocean system [13]. All the snow and atmospheric parameters that affect the bidirectional reflectance of snow/ice and their sensitivities were investigated. The results showed that reflectance of snow/ice was highly anisotropic with the strongest reflectance in the forward scattering directions, especially under conditions of low solar elevation typical at high latitudes. In this paper, the theoretical results from Part I provide a basis to analyze the bidirectional reflectance of a number of AVHRR channel 1 and channel 2 images of snow-covered sea ice acquired in the Arctic. In Section II of this paper, some AVHRR images are presented that show the dependence of the satellite-observed reflectance of snow on the geometry (i.e., solar zenith, relative azimuth, and view angle). In Section III, the radiative transfer model is used to simulate the anisotropic reflectance of snow over sea ice observed at the top of atmosphere and to develop an anisotropic correction method for it. Section IV presents the operational algorithm for anisotropic correction and results obtained by applying it to AVHRR imagery. Conclusions from this study are given in Section V.

The authors are with the Digital Image Analysis Laboratory, Scripps Institution of Oceanography, University of California, San Diego, La Jolla, CA 92093-0237 USA (e-mail: jsimpson@ucsd.edu).
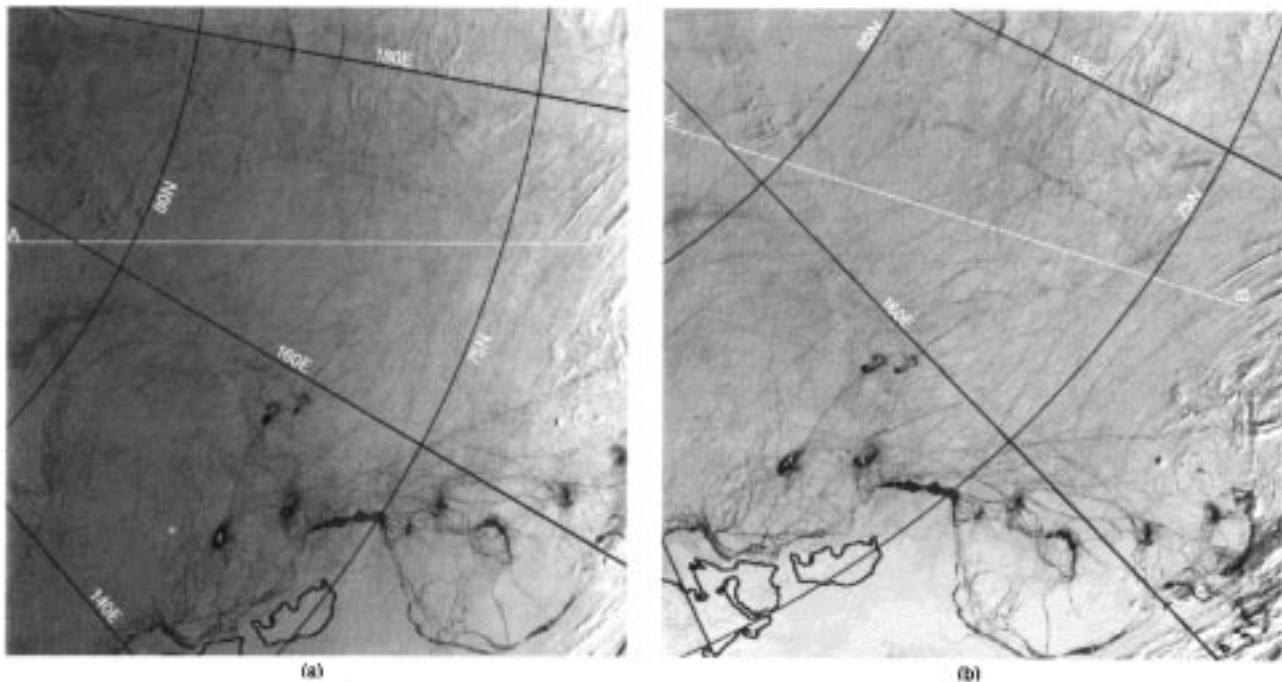
Fig. 1.   Two AVHRR channel 2 images of isotropic albedo (reflectance) acquired over the Chukchi Sea in the Arctic by two different satellites with different view geometry but with close pass times (a) from NOAA 12 and (b) from NOAA 14. The line from A to B crosses the same locations in both images.

II. BIDIRECTIONAL REFLECTANCE OF SNOW OBSERVED FROM AVHRR

The bidirectional reflectance of snow can be seen in Arctic AVHRR imagery. All the data used in this study are high resolution picture transmission (HRPT) data, which have a nadir resolution of 1.1 km. Fig. 1 shows two images of AVHRR channel 2 reflectance. These images were taken only 10 min apart over the Chukchi Sea on April 5, 1996, but from different satellites. Image (a) is from NOAA 12, and image (b) is from NOAA 14. These two satellites have almost identical AVHRR channel specifications [14]. Based on the postlaunch calibration of the NOAA 14 satellite by Rao and Chen [15], for a given raw pixel count C_i in channel i, the reflectance (or equivalently, the isotropic albedo) α_i in percent is given by

$$\alpha_i = S_i(C_i - C_0)\rho^2 / \cos\theta_0 \tag{1}$$

where C_0 is the offset (41 in both channels 1 and 2), θ_0 is the solar zenith angle, and ρ is the Earth-Sun distance in astronomic units. S_i is the calibration slope given by (4) and (5) in [15], which is a function of day number d after the launch of the NOAA 14 satellite and is expressed as

$$S_1 = 0.0000232d + 0.109 \tag{2}$$
$$S_2 = 0.0000373d + 0.129 \tag{3}$$

for channel 1 and channel 2, respectively. The reflectance given by (1) equals the actual albedo if and only if the reflecting radiance is isotropic or the view angle is independent. Thus, this reflectance is also called the isotropic albedo.

Because no postlaunch calibration for NOAA 12 is available, and in order to make the radiance from the two different satellites comparable, we have cross-calibrated the NOAA 12 data using the postlaunch calibration for NOAA 14 given in [15]. The calibration for NOAA 14 above is transferred to NOAA 12 by using a colocated nadir observation method [16]. In this cross-calibration method, the nadir location (where the two satellite passes cross each other) is identified based on their orbiting equations. If the neighborhood around this crossing point has uniform snow, then the scene can be used as a cross-calibration site. The neighborhood is made small so that all the pixels in it have close to nadir viewing conditions. A neighborhood size of 20×20 pixels is used in this study. The two satellite passes are also constrained to have their pass times over the calibration scene as close to each other as possible (e.g., Fig. 1). Thus, both satellites view the common calibration site with almost identical viewing geometry (i.e., nadir viewing with similar solar zenith angle) and common atmospheric and snow conditions. Therefore, the reflectance observed by the two satellites for such a scene should be the same regardless of the anisotropic reflectance. The calculated ratio of the postlaunch calibrated NOAA 14 reflectance and the prelaunch calibrated NOAA 12 reflectance (NOAA 14/NOAA 12) at the calibration site are then used to convert the prelaunch NOAA 12 reflectance to a postlaunch reflectance, which thus has the same scale as the NOAA 14 postlaunch reflectance.

In Fig. 1, the sensor scan direction, which is perpendicular to the satellite nadir track, is horizontal for the image plane in (a), but it is vertical for (b). Because the two images were collected only 10 min apart, we can expect that the atmosphere and the snow have not changed much during this short period and therefore, the isotropic albedo of snow observed by the two satellites should be nearly identical if the effect of view angle or the bidirectional reflectance is negligible. Actually, even the cloud structures do not show visual differences between the two images. These facts indicate that the reflectance or the isotropic

ISOTROPIC ALBEDO FROM PASS (a)
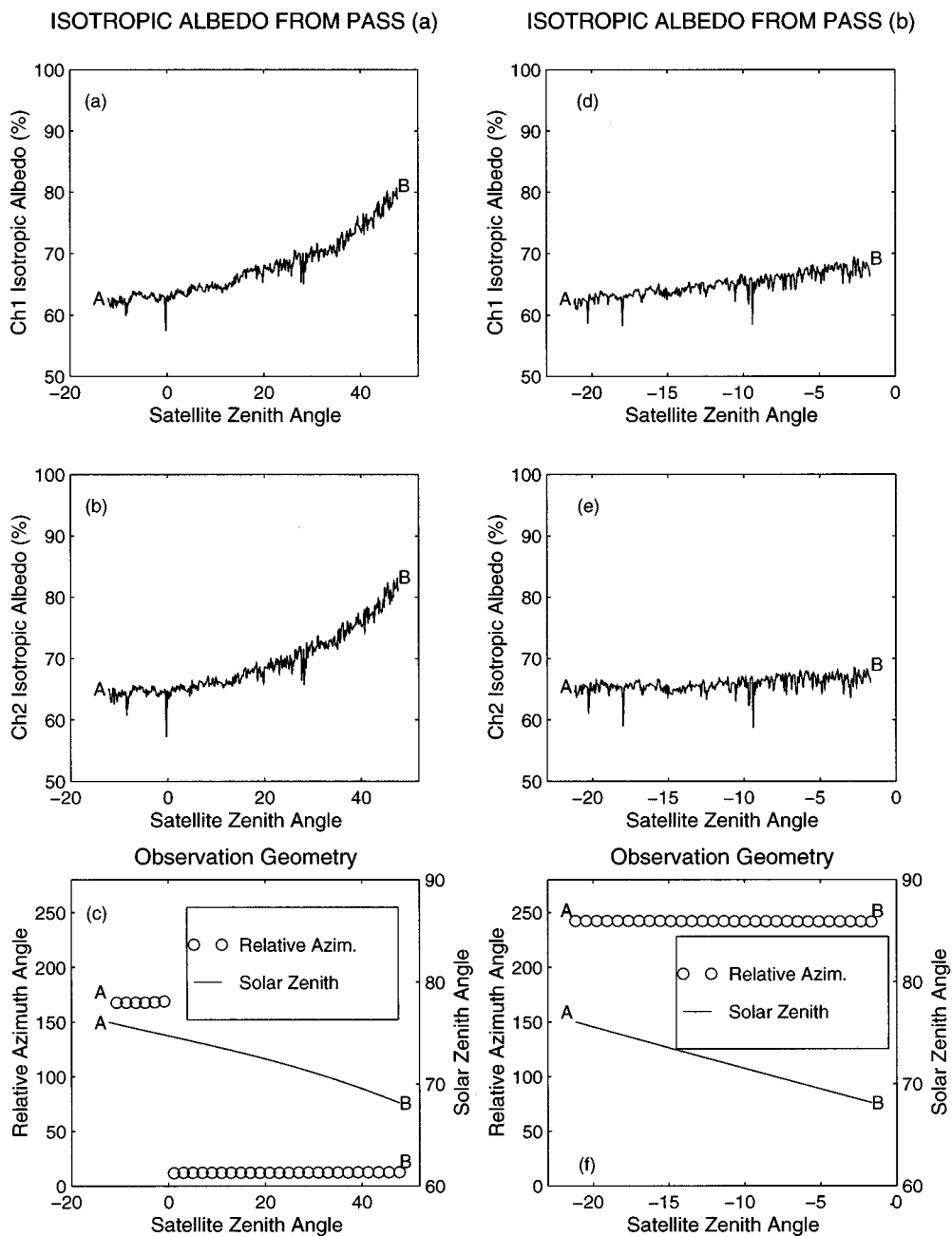
ISOTROPIC ALBEDO FROM PASS (b)

Fig. 2. Satellite-observed isotropic albedo of AVHRR channels 1 and 2 and view geometry along the line from A to B marked on the images in Fig. 1. The left three panels are for the satellite pass (a) and the right three panels are for the pass (b) shown in Fig. 1.

albedo, assuming no angular dependence, should be similar for a common snow target in the two images, though some atmospheric effects exist. These two images, however, show very different reflectance patterns. For example, in (a), the isotropic albedo increases from the left side to the right, whereas in image (b), the isotropic albedo is much more uniform across the entire image.

To illustrate this anisotropic characteristic of snow reflectance, a scan line labeled from point A to B on image (a) has been selected. This same line is also mapped on image (b) using accurate registration and navigation. The isotropic albedo observed from the two satellites and its relationship with the satellite zenith angle (view angle), as well as observation geometry along this selected line, are shown in Fig. 2.

Panels (a) and (b) show that, except for some occasional sudden decreases, which are believed to be caused by contamination from leads, cracks of snow and ice or even small clouds, the isotropic albedo observed in pass (a) presents a systematic increase from point A to B in both AVHRR channels 1 and 2. The isotropic albedo from A to B observed from NOAA 14 (panels d and e), however, shows a slight increase for channel 1 and almost no systematic variation in channel 2. Comparing panel (a) with (d), and (b) with (e), it is clear that, contrary to expectation, both the isotropic albedo and its variation from A to B for the two near simultaneous observations are not the same or even similar. Because the viewing conditions are nearly simultaneous and the satellite cross-calibration was applied, variations in snow and
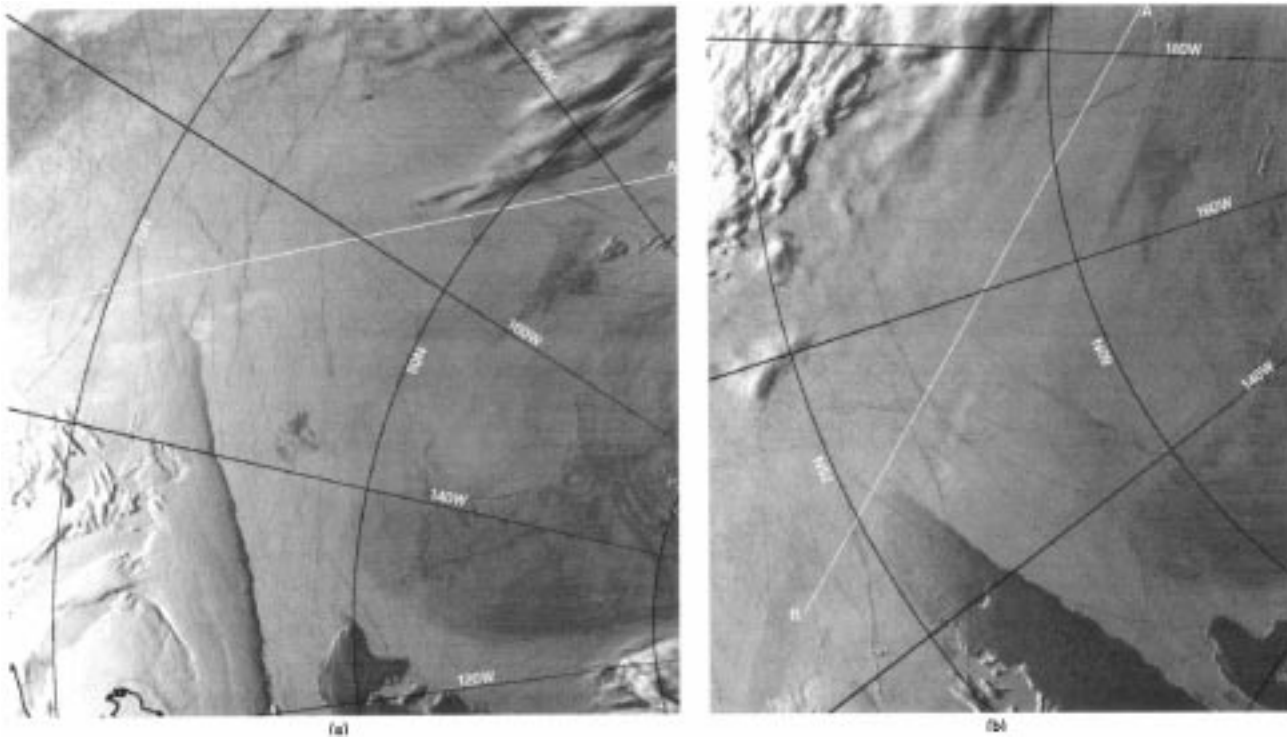
Fig. 3. Two AVHRR channel 2 images of isotropic albedo acquired over the Beaufort Sea by the same satellite (NOAA 12) but taken about 3 h 14 min apart. The line from A to B has the same geolocations on both images.

atmosphere and calibration uncertainty can be excluded as causes for these observed differences in the isotropic albedo. These differences, in fact, would be larger if it were not for the blurring or smoothing effect from scattering by the atmosphere, which reduces the strong forward scattering peak and hence the reflectance anisotropy observed at the TOA [13]. These differences can only be explained by the different viewing geometry of the two observations.

Although the solar zenith angles are similar, the satellite zenith (view angle) and the relative azimuth angles (the azimuth difference between the satellite view zenith plane and the solar zenith plane) are very different for the two scenes [Fig. 2(c) and (f)]. The line from A to B in image (a) covers a much wider range of view angles than in image (b). In image (a), the satellite view angles change from the backward scattering direction (when satellite zenith angle < 0) to a large forward scattering direction (when satellite zenith angle > 0). In addition, the relative azimuth angles are close to the principal plane (the plane containing the sun, the target, and the zenith). Based on the theoretical analysis by [13], under these viewing conditions, the reflectance of snow is most highly anisotropic. For pass (b), the view angles are limited to the backward scattering region, and the relative azimuth angle (around $250°$) is far away from the principal plane. The theoretical study [13] also showed that under such observation angles, the angular dependence of snow reflectance is very small. Thus, the small reflectance variation observed under the viewing geometry of pass (b) is expected. The small increase of the channel 1 isotropic albedo from A to B observed in pass (b) is most likely due to atmospheric effects. Higher scattering occurs in the channel 1 spectral region due to shorter wavelengths.

The calibrated channel 2 isotropic albedo at the top of the atmosphere (Fig. 2) also shows slightly higher values than that of channel 1. This probably is not correct because snow has higher albedo in the visible spectrum (channel 1) than in the near infrared (channel 2) and because the atmosphere tends to attenuate more radiation in channel 2 than in channel 1. Based on our model results, the degradation of the sensor response in NOAA 14's postlaunch calibration for channel 2 reported in [15] is likely to be overestimated and therefore, the channel 2 reflectance is overestimated.

Fig. 3 shows another pair of images taken on March 29, 1996 over the Beaufort Sea. These two images were taken by the same satellite sensor with pass (b) 3 h 14 min later than pass (a). Although the clouds have moved and changed during the time period between the two images, we cannot see any visible movement in the structure of the leads. A common target line, which has the least cloud contamination in both images, was selected to show the anisotropic feature of snow reflectance at the top of atmosphere. Fig. 4 shows the isotropic albedo from A to B and the observation angles for both passes. Panels a, b, d, and e show that both passes observed a systematic variation of snow reflectance from A to B, but the observation from pass (a) shows a much stronger anisotropic characteristic than pass (b). These differences are mainly caused by different sun-satellite geometry (panels c and f). Both observations show a systematic increase of reflectance from A to B because both observations covered a large range of forward view angles and are close to the principal plane. The stronger angular variation observed for pass (a) occurs because it has an even wider range of viewing and solar zenith angles. Different solar zenith angles cause different atmospheric paths and hence different scattering of solar radi-

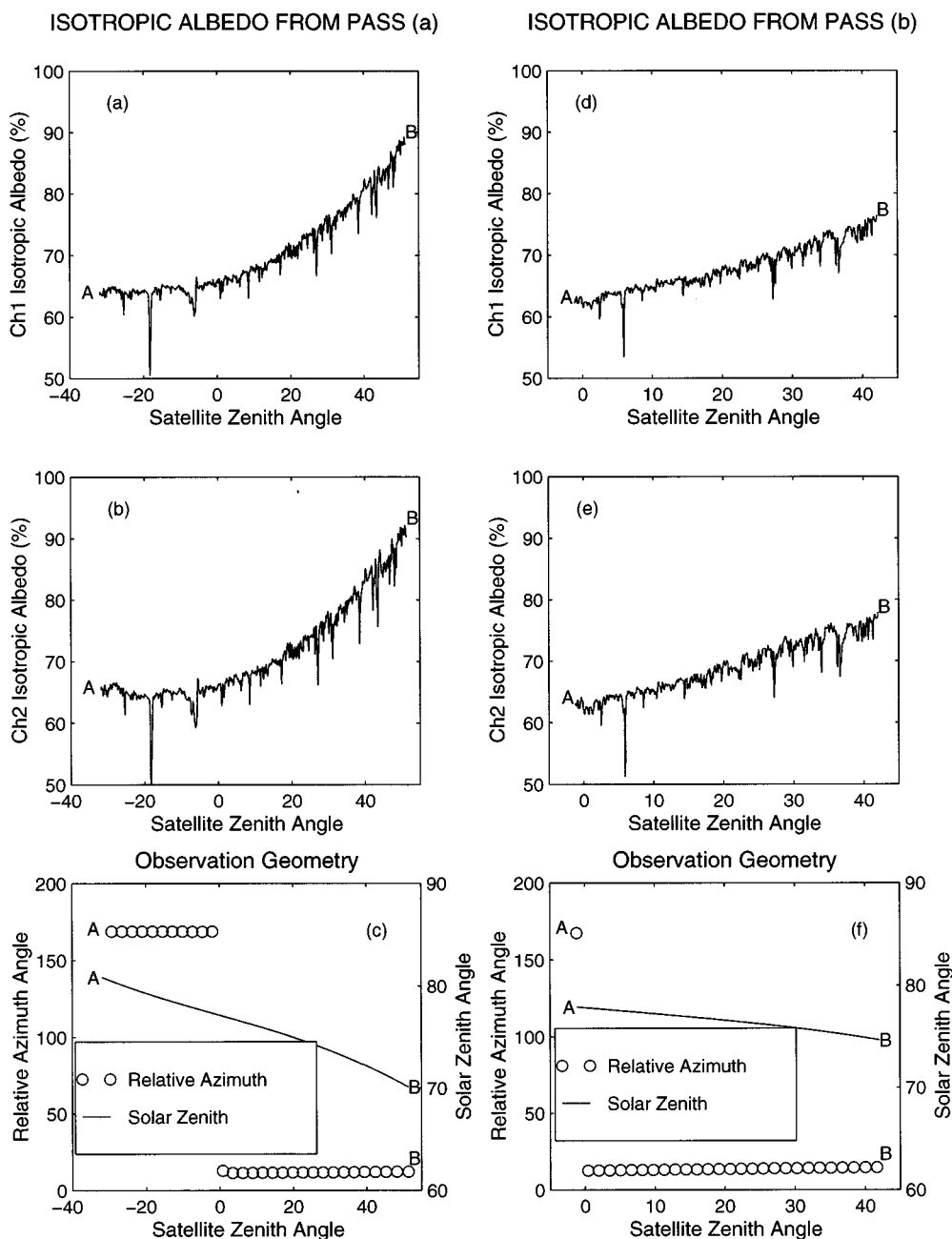ISOTROPIC ALBEDO FROM PASS (a) ISOTROPIC ALBEDO FROM PASS (b)

Fig. 4. Same as Fig. 2, but for the two satellite passes in Fig. 3.

ation. Fig. 4 also shows that channel 2 reflectance has a larger variation with the satellite view angle, or a more anisotropic reflectance pattern than that in channel 1. This is consistent with the model prediction of [13].

Strong anisotropic reflectance of snow is also observed in many other images (e.g., Fig. 5). This image was collected over the Chukchi Sea on April 5, 1996 (panel 5a). Panel (b) shows the channel 1 reflectance observed from space along the selected scan line labeled on the panel (a) image. Channel 2 reflectance shows a similar pattern and is not presented. Panel (c) shows the observation geometry for pixels on the selected line. Again, due to view geometry effects, the image shows snow that appears darker on one side of the scene than on the other. As expected, we also see a higher isotropic albedo at large view angles. How-

ever, because the isotropic albedo is derived directly from the observed radiance (1) and it does not account for anisotropy, this albedo cannot be used to represent the actual energy reflected to space.

III. MODEL SIMULATION AND ANISTROPIC CORRECTION

Figs. 1–5 clearly show the effects of observation geometry on snow reflectance observed from space. First, the actual *in situ* snow albedo from location A to B in these images should not have such a large variation because the images were taken in late March or early April, when snow melt has not yet started in the Arctic and the surface is covered mostly by new snow, which has uniformly high albedo. Second, the snow albedo ob-
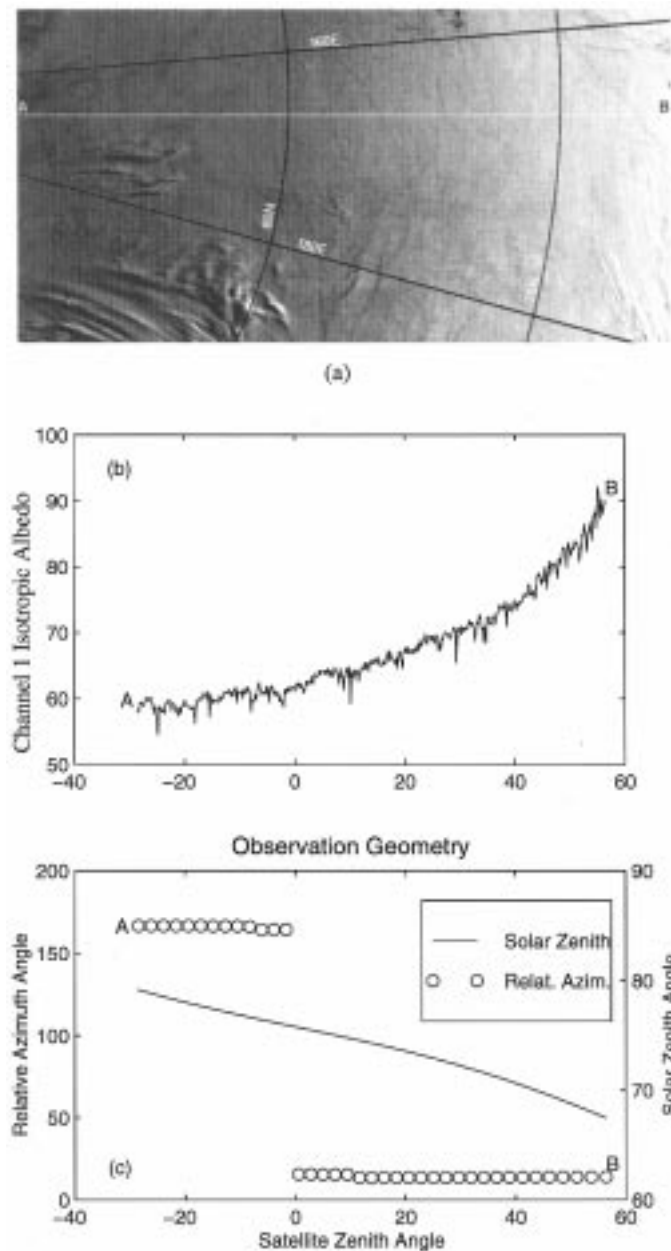
Fig. 5.　An observation by NOAA 12 over the Chukchi Sea on April 5, 1996. (a) Channel 1 image of isotropic albedo, (b) channel 1 isotropic albedo with satellite view angle along the scan line from A to B labeled on the image, and (c) observation angles for the selected line.

served under clear sky conditions within a short time period but from different satellite passes also should not be as different as shown above due to similar snow and atmospheric conditions. Clearly, to avoid inaccurate retrieval and misleading interpretation of snow albedo derived from satellite data, the angular effects of bidirectional reflectance on the observations must be corrected.

In this section, the strong angular variations presented in Section II are used as examples for model simulation and anisotropic correction. First, we directly model the isotropic albedo or reflectance observed by the satellite. If the angular variation of reflectance can be simulated, then the angular correction for it is straightforward. Consistent with the derivation

of the isotropic albedo from satellite radiance [15], we first calculate the radiance $I(\theta_0, \theta, \phi)$ at direction (θ, ϕ), where θ_0, θ, and ϕ represent the solar zenith, the view zenith, and the relative azimuth angles, respectively. Then, the modeled isotropic albedo is given as

$$\alpha_i(\theta_0, \theta, \phi) = \frac{\pi I(\theta_0, \theta, \phi)}{F \cos \theta_0} \quad (4)$$

where F in (4) is the solar irradiance at the TOA. In the model computations, the radiance and irradiance are integrated and weighted by the spectral response function of the specific AVHRR channel [14]. Together with the radiance, the Anisotropic Reflectance Factor (ARF) can be derived simultaneously

$$\text{ARF}(\theta_0, \theta, \phi) = \frac{\pi I(\theta_0, \theta, \phi)}{F_u(\theta_0)} = \frac{\alpha_i(\theta_0, \theta, \phi)}{\alpha(\theta_0)} \quad (5)$$

where F_u is the upward flux and $\alpha(\theta_0)$ is the actual albedo, independent of view angles. As shown in (5), ARF is also equivalent to the ratio of the isotropic albedo and the actual albedo. Thus, it represents the departure of the reflected radiation field from an isotropic distribution and is one if the reflection is isotropic. Therefore, the satellite-derived isotropic albedo, divided by the ARF, gives the actual TOA albedo (or equivalently, the anisotropy-corrected albedo).

A coupled radiative transfer model for the atmosphere, snow/ice, and ocean system has been used for this model simulation [17], [18]. Because the coupled model treats the snow, ice, and ocean as different atmospheric layers, and the radiative transfer equation was solved in the coupled system consistently, there is no need to assume any radiance distribution at the interfaces or at the surface [18]. Therefore, it is more consistent and accurate than the decoupled modeling approach. The mathematical representations of the radiative processes in this model have been confirmed by model-model comparisons [19] and self-consistency tests [18]. The comparison with other models (most of them were implemented by the Monte Carlo technique) in [19] showed that for the same model input specifications, our model gives the same results for radiance and irradiances as other models. Some validations of the radiative transfer model by measurements of snow/ice reflectance are given in [13] and [17]. Validations by observational data in the atmosphere can be found in [20]–[22]. However, it should be noted that all these measurement-based validations are incomplete due to limitations in the completeness of measured parameters.

The angular input parameters for the model are obtained directly from the satellite ephemeris data and orbit models. A simplified two-layer model for snow with total thickness of 20 cm is used. The snow below this level, however, has little or no effect on the albedo in AVHRR channels 1 and 2, because almost no radiation can reach this depth and therefore, the parameter specifications for the sea ice and ocean underneath are not needed. To date, there has not been a large-scale effort to systematically measure the snow cover thickness on sea ice in the Arctic ocean. Based on a few isolated studies, this assumed thickness of 20 cm is likely to be less than most actual snow depths on sea ice in
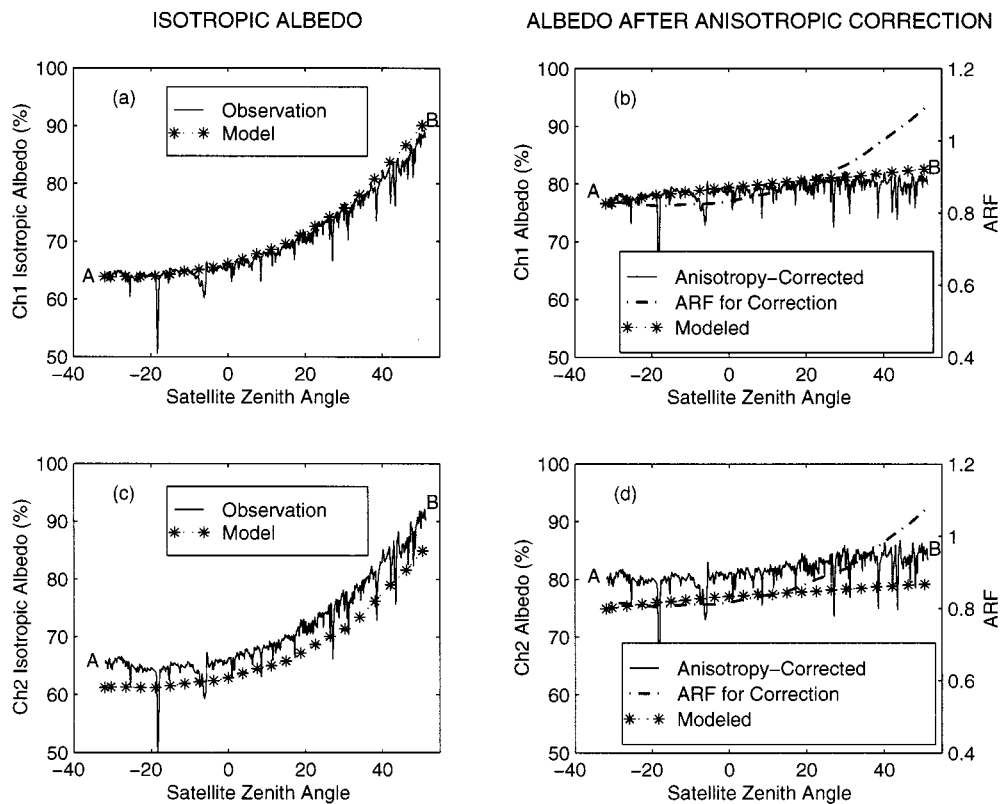
Fig. 6. Model-observation comparisons for albedo along the line from A to B labeled in image (a) in Fig. 3. Panels (a) and (b) are for AVHRR channel 1 and panels (c) and (d) are for channel 2. Panels (a) and (c) show the comparison of TOA isotropic albedo for channels 1 and 2, respectively. Panels (b) and (d) show the comparison of the TOA albedo after anisotropic correction. The correction coefficient function, ARF, is also shown.

the Arctic spring when the images being studied were collected [23]–[25]. It should be noted that the assumed 20 cm of snow depth is a very conservative number for an optically semi-infinite surface. In fact, our calculations showed that only a few centimeters of snow cover could be considered as semi-infinite for channel 2 radiation and 10 cm of new snow on sea ice has essentially the same albedo as a 20 cm of a layer of snow. If occasionally the snow is extremely thin such that the reflectance will be largely reduced and is significantly less than the surrounding snow, then this snow pixel is excluded from the analysis.

According to Tucker *et al.* [26], the snow cover over Arctic sea ice is fairly simple and it consists primarily of wind-blown, hard-packed snow composed of well- rounded grains. In the model simulations, the 10 cm of the upper layer of snow are assumed to have a mean grain radius of 0.1 mm, consistent with the new/fresh snow conditions of the early Arctic spring. The lower layer is assumed to have a mean grain radius of 0.3 mm for old snow [26]–[28]. These assumed values may not be the same as the actual ones. Our sensitivity tests, however, showed that the errors in the assumed values of these snow parameters have a relatively small effect on the TOA albedo in the spectral regions of AVHRR channels 1 and 2 for optically thick snow for this Arctic season [13]. This is especially true when such errors are compared with other potential error sources (e.g., satellite calibration). Doubling the snow thickness to 40 cm or doubling the grain size in the lower layer, for example, gives essentially identical results. Of all these parameters for snow, the grain size in the upper layer has the largest relative effect on the calculated

albedo. But within the grain-size range for new snow (0.02 to 0.1 mm in radius), the error due to inaccurate grain size is also small in both AVHRR channel 1 and 2.

Measurements of snow reflectance in the Antarctic by Warren *et al.* [29] showed that the sastrugi (wind-formed roughness on the snow surface) has an effect on snow reflectance, but they also indicated that the effect is mainly for large view angles ($>50°$) in the forward scattering direction and when the sastrugi is oriented near perpendicular to the solar beam. It should be noted that the maximum satellite scan angle for AVHRR is $54°$ (the corresponding maximum view zenith angle is $69°$), and actually most of the pixels in images we analyzed have view zenith angles of less than $50°$. In addition, the observed sastrugi in [29] is of order 1 m in width and a few meters in length, while the scale for each AVHRR pixel is 1.1 km. Lacking observation data for possible sastrugi of snow on sea ice in the Arctic ocean (e.g., their heights, widths, orientations, and distributions in each pixel range), we will not consider this roughness effect in this study.

To simplify the computation and save computation time, the scattering phase function of snow is approximated by a two-component Henyey-Greenstein phase function as

$$P(\Omega) = 0.8F(g_1, \Omega) + 0.2F(g_2, \Omega) \tag{6}$$

where Ω is the scattering angle and $F(g, \Omega)$ is the Henyey-Greenstein phase function with asymmetry factor g. In (6), g_1 is specified as 0.88, around the value of the asymmetry factor of
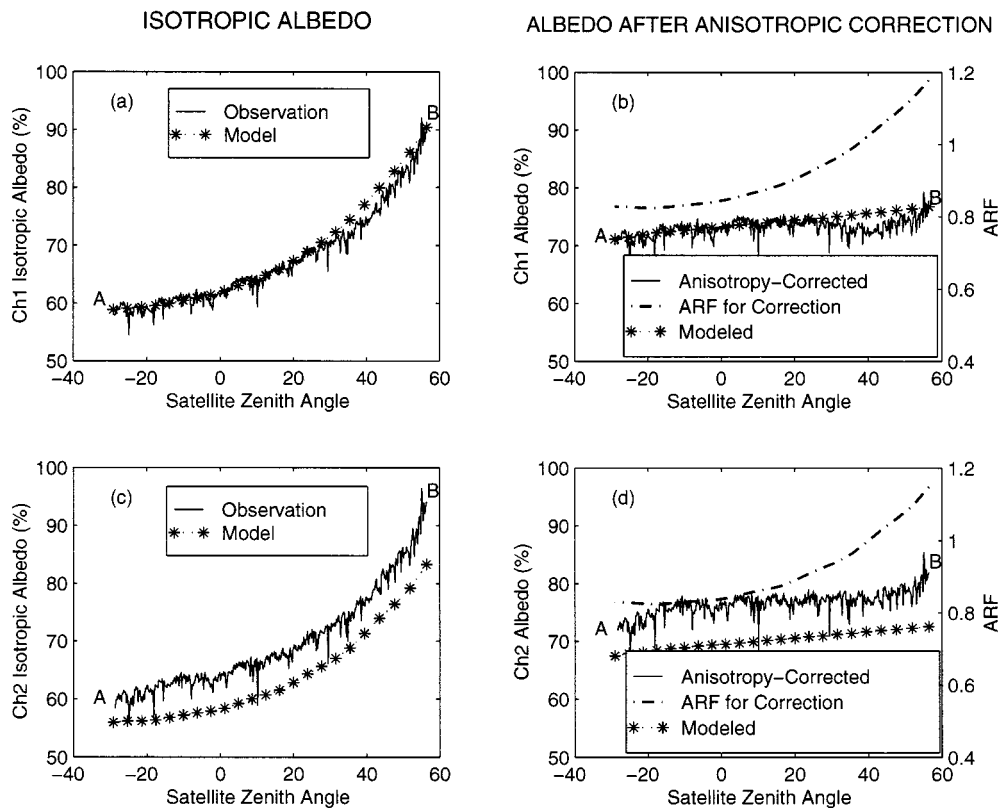
Fig. 7. Same as Fig. 6, but for the observation in Fig. 5.

snow in the visible and near-infrared spectrum [27], [30]. According to [30], the asymmetry parameters for densely packed particles are very close to those for independently scattering spheres and may be used in practical computations for densely packed grains such as snow. The value of g_2 is specified as -0.1 to account for the small backward scattering peak of snow, which has been demonstrated in theoretical computations and in many field observations of snow bidirectional reflectance (e.g., [31]–[33], [29]). For example, Figs. 3 and 4 in [29] show a backscatter peak at the back view angle of around $65°$. However, direct comprehensive measurements of the snow phase function have not yet been conducted. Thus, the exact formula to represent the snow phase function, including the backscattering, is still unknown. Therefore, the formulation used here (6) is an approximation based on theoretical computation and indirect field observations.

Although the aerosol or haze loading is small in the Arctic compared with that of the low latitudes, the Arctic haze might have a non-negligible effect on the magnitude of the TOA albedo, especially in AVHRR channel 1. Lacking *in situ* observation data, we determine the haze optical depth by matching the model computation with the satellite observed radiance at nadir viewing in channel 1.

The isotropic albedo along the line from A to B in Fig. 3(a), which was shown in panels (a) and (b) of Fig. 4, will be used as the first example for modeling and anisotropic correction for the TOA snow albedo. The results of such a model-observation comparison and anisotropic correction are presented in Fig. 6. Panels (a) and (c) in Fig. 6 show that the variation in satellite-observed isotropic albedo with view

zenith angle has been matched fairly well by model results, although there is an offset between the modeled and observed isotropic albedo in channel 2. This offset is very likely from the calibration error described above. The calibration by (2) and (3) makes the TOA snow reflectance in AVHRR channel 2 similar or even larger than that in channel 1, which is practically impossible. The only other factor that might be able to produce such a big disagreement between model and observation in AVHRR channel 2 is the snow grain size, because the snow reflectance increases as snow grain size decreases. However, the specified grain size (0.1 mm in radius) in the model simulation was already low to represent the new snow in the Arctic spring. Even reducing this size by half increases the TOA albedo by less than 2%, much less than the offset (larger than 5%). Increasing the grain size produces the opposite effect. Therefore, the assumed snow grain size can be excluded as the cause for this channel 2 offset.

Panels (b) and (d) in Fig. 6 compare the anisotropy-corrected albedo derived from satellite data (5) with the modeled albedo. The ARF used for correcting the satellite-observed reflectance is also shown in these two panels. The modeled albedo is calculated from the upward and downward fluxes directly and is not derived from ARF. The small variation in the modeled albedo along the selected line from A to B is due to the variation in the solar zenith angle. There is a good agreement between model and corrected albedo observed in channel 1, and there is an offset in channel 2. More importantly, panels (b) and (d) show that the snow albedo becomes more uniform after correction, which indicates that most, if not all, of the angular effects have been eliminated successfully.
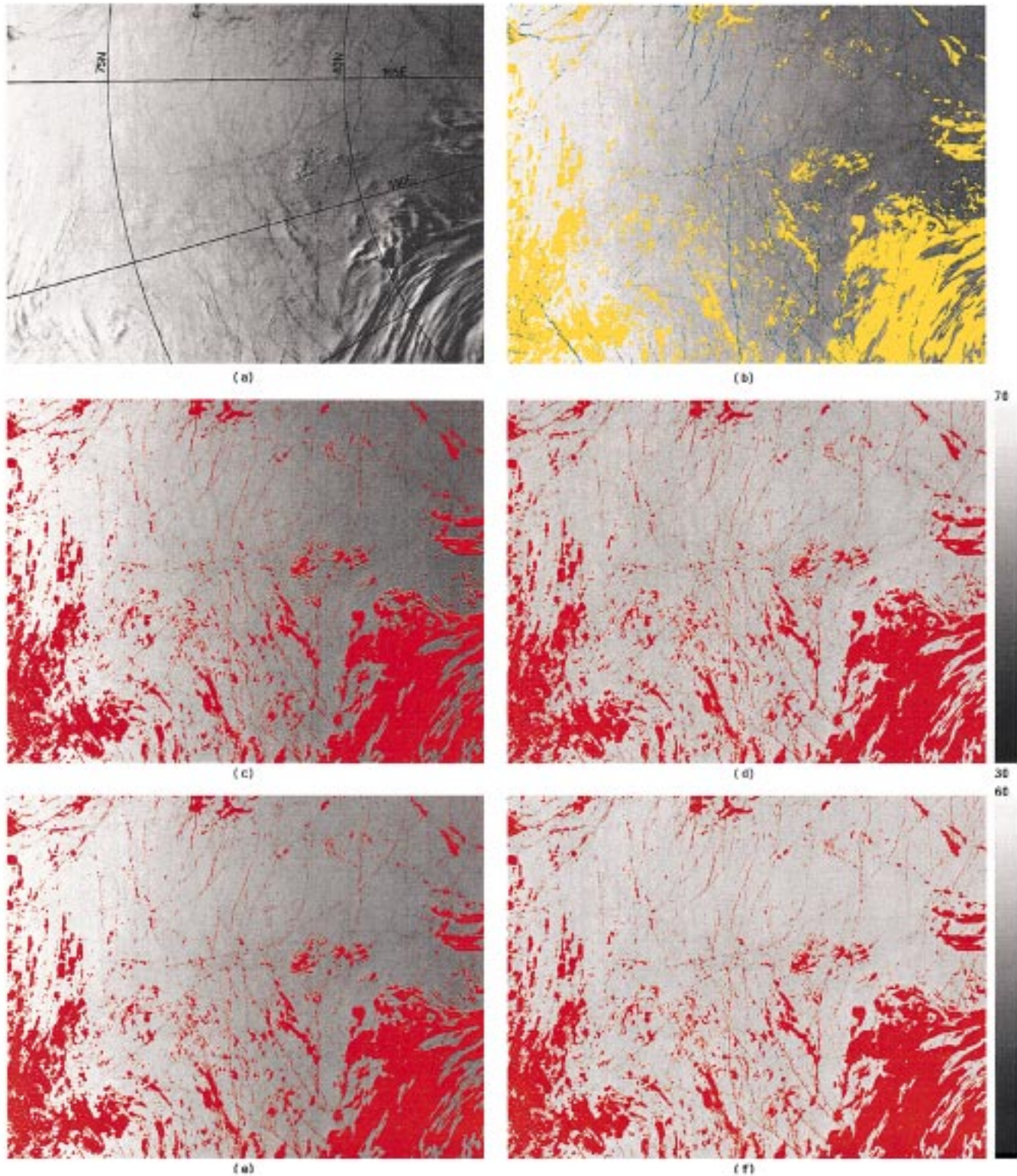
Fig. 8.   Image acquired over the Chukchi Sea on April 5, 1996. (a) Histogram equalized channel 1 isotropic albedo; (b) same as (a), but with leads and lead-contaminated pixels represented by blue and clouds represented by yellow; (c) AVHRR channel 1 isotropic albedo of snow; (d) Channel 1 snow albedo after anisotropic correction; (e) Channel 2 isotropic albedo; and (f) Channel 2 albedo after anisotropic correction. The red overlay in panels (c)-(f) are all the pixels that have been excluded because they are not 100% snow (blue and yellow in panel b). The albedo scale for channel 1 (panels c and d) is represented by the wedge to the right of panel (d) and for channel 2 is placed to the right of panel (f).

Similar to Fig. 6, Fig. 7 shows the model-observation comparison and anisotropic correction results for the A-B line from the image in Fig. 5. Again, the systematic variation due to the

observation angles has been eliminated after the anisotropic correction. At large view angles in the forward scattering direction, the albedo derived from satellite observation in channel 1
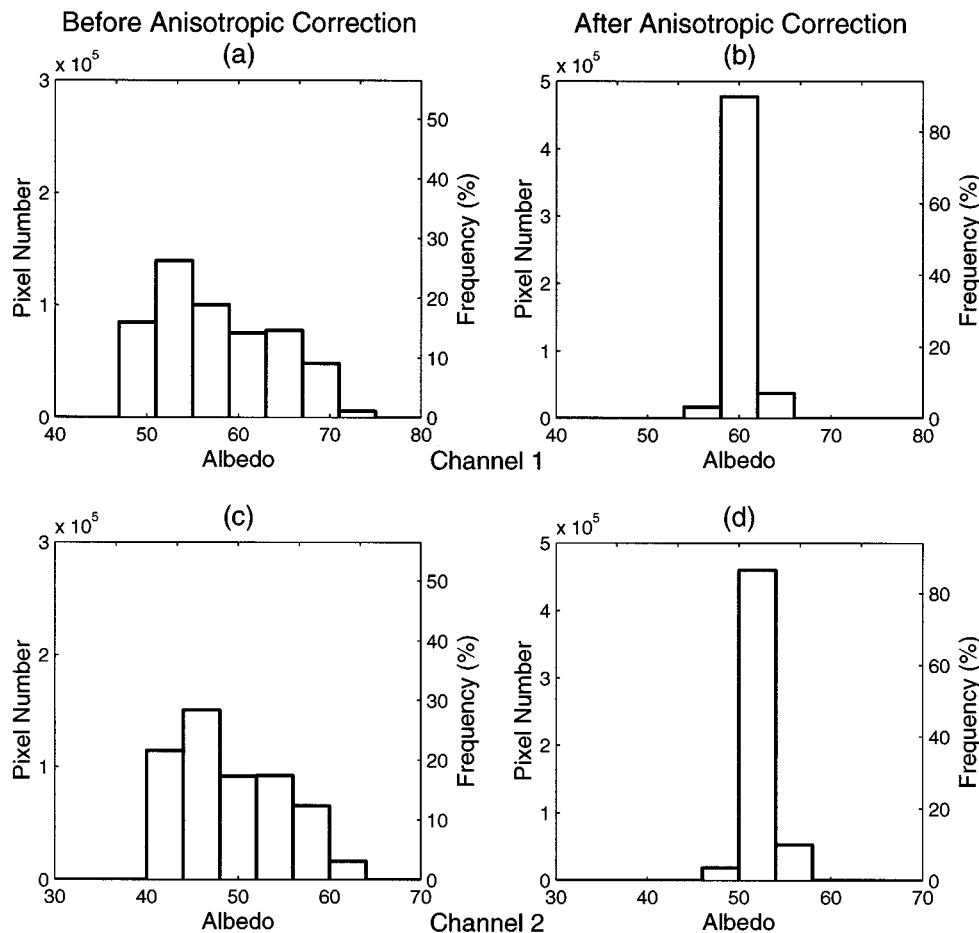
Fig. 9. Histograms for snow albedo before and after the anisotropic correction. Panels (a)–(d) correspond to images in panels (c)–(f) in Fig. 8, respectively.

tends to be smaller than the model prediction in all examples shown. The same applies to the albedo in channel 2 if the offset is excluded. Results from other data sets (not presented) also showed this model-observation difference at large view angles. Generally, for larger view angle, this difference also becomes larger. There are a number of possible causes for this. First, there might be imperfect physics in the model and/or the assumptions used to characterize the physical properties of the snow and atmosphere. The model might simply overestimate the reflectance at those large angles due to inaccurate treatment of the optical properties of the atmosphere and snow (e.g., the phase function). Second, the assumed uniformness for snow properties along the lines studied also may not be exact. In particular, because the snow at large view angles happens to be closer to the coast, the actual snow there might not be as clean as in the Arctic interior due to pollution contamination. Another cause might be the sastrugi: the wind-formed snow surface roughness. Warren *et al.* [29] found that this meter-scale roughness could reduce the snow reflectance, particularly at large viewing angles in the forward-scattering direction.

IV. APPLICATION OF ANISOTROPIC CORRECTION TO IMAGERY

In Section III, the approach for anisotropic correction of the viewing/illumination geometry effect has been demonstrated,

but it was applied only to a single scan line in the images and was based on a time-consuming pixel-by-pixel computation. To apply this correction over an entire image, such a pixel-by-pixel computation is impractical, if not impossible. Therefore, a pre-calculated look-up table of ARF, the correction factor, was created and used for the operational anisotropic correction algorithm. This table contains ARF values for various solar zenith angles, satellite zenith angles, relative azimuth angles, snow properties, and haze loadings, which were shown to be the most sensitive parameters for ARF [13]. Once the snow properties and haze loading are specified as described above, the ARF to be applied to each pixel in an image can be retrieved from the look-up table based on the angles derived from satellite orbit data. If any of the parameters to select the ARF do not match the tabulated entries, then interpolation can be done. The table, however, has sufficient angular resolution to retain high accuracy if interpolation is needed. This table is too large to include herein, but it is available from the authors upon request. This implementation greatly reduces the execution time for the anisotropic correction process. For example, the anisotropic correction on a 1000×1000 pixel image requires only a few minutes when the look-up table is used.

Of course, before the correction is applied to an image, it is necessary to first identify the snow pixels without cloud or leads contamination. In late March and early April, when the images studied in this paper were collected, it is still snow season
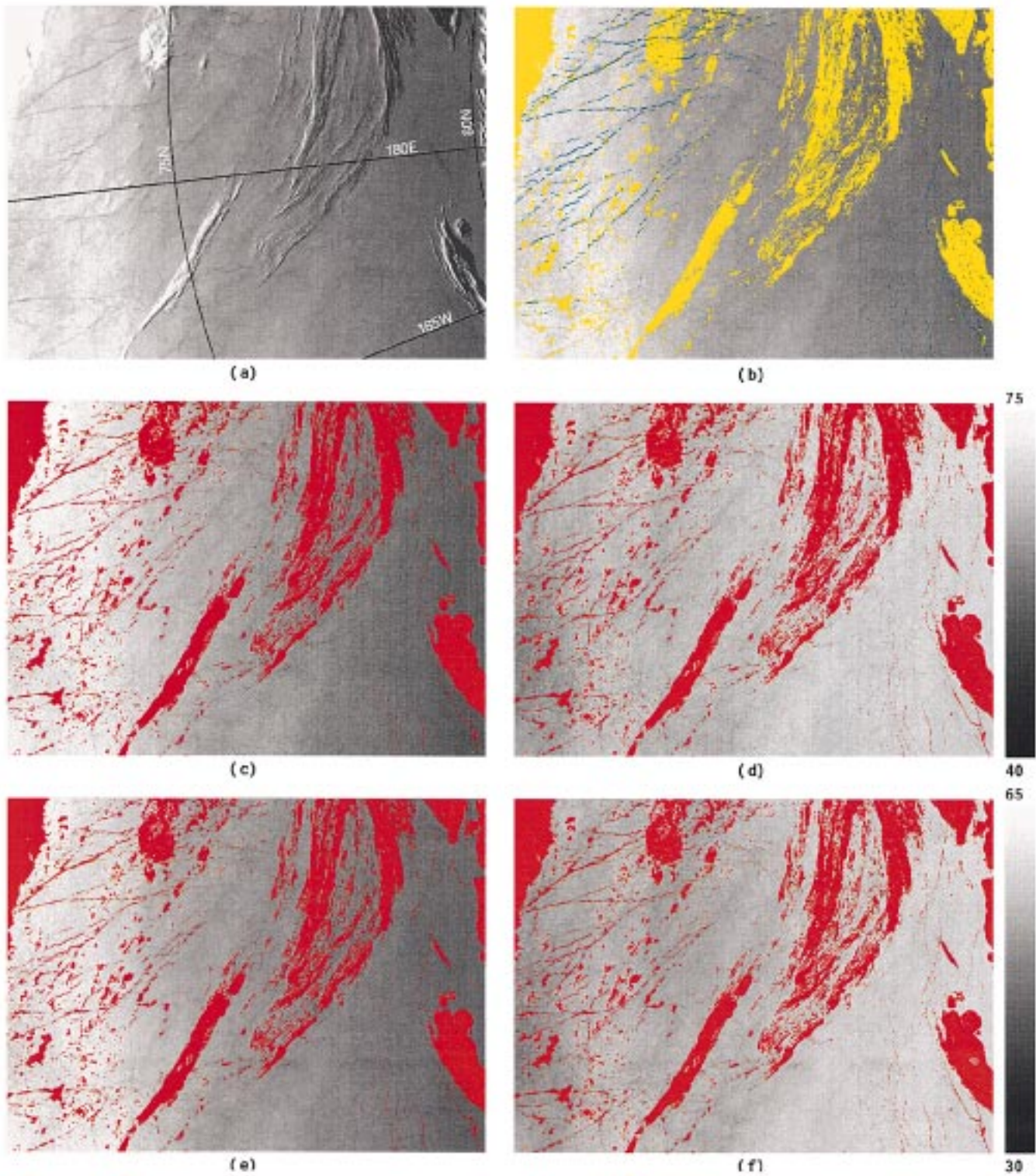
Fig. 10.   Same as Fig. 8, but for an image taken north of the Bering Strait in the Arctic ocean on March 26, 1997.

in the Arctic, and the snow has not yet started to melt. Except for small areas of open water, leads and occasional young ice, the pixels in Arctic imagery are either snow-covered ice or clouds. Therefore, to properly identify the snow pixels, one must exclude clouds and leads. Leads and open ocean are easy to identify in AVHRR imagery based on their channel 1 or 2 albedo and channel 4 or 5 temperature. Leads and open ocean

have lower albedo but higher temperature than the surrounding snow or clouds. The open ocean is first detected by applying a threshold to channel 1 or channel 2 reflectance. Then, by comparing the channel 2 reflectance and the channel 4 temperature with their 9×9 window averages, respectively, pixels with 6% lower reflectance and with 6% higher temperature are classified as leads or leads contaminated. After the open ocean and leads
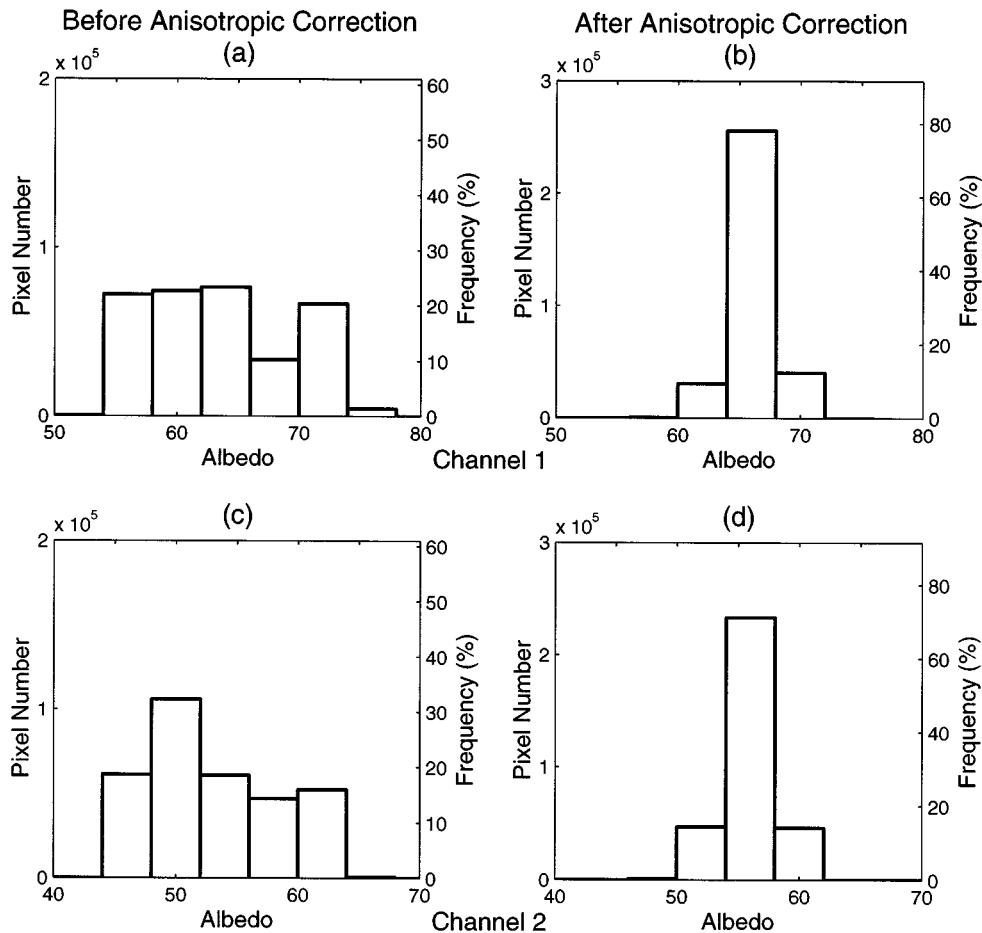
Fig. 11. Same as Fig. 9, but for images in Fig. 10.

are excluded, cloudy pixels are discriminated over the remaining image pixels, which are either snow, cloud, or snow-cloud mixture. Clouds and snow have different structure. Cloud pixels, however, can have similar albedo and/or temperature to those of the surrounding snow. Also, the albedo of some cloudy pixels can be either substantially higher or lower than that of snow. Generally, clouds have a higher statistical standard deviation for albedo and temperature than snow within a domain. Based on these facts, clouds are identified using these statistical features. However, this simplified method cannot be taken as an accurate cloud classification. Specifically, the identified cloud area is generally larger than the actual cloud area. In other words, some snow pixels, particularly those close to the cloud edge, will be assigned as cloud based on this approach. This conservative classification is acceptable for the present study, however, as long as the snow class assignment is correct. As the examples below show, this approach provides good cloud and leads free scenes for the anisotropic correction.

Fig. 8 is an image acquired over the Chukchi Sea by NOAA 12 on April 5, 1996. Panel (a) is channel 1 isotropic albedo at the TOA. It was histogram equalized so that the leads structure and cloud edges could be better visualized [34]. Panel (b) is the same as panel (a), except the blue represents the leads or leads contaminated pixels and the yellow represents clouds. The identified leads and clouds are consistent with the visualized leads and clouds in panel (a). It also shows that a small number of

snow pixels by the cloud edges have been assigned to clouds (but not the opposite case, which is undesirable for this study). Panel (c) is the channel 1 isotropic albedo at the TOA based on prelaunch calibration for NOAA 12. The red represents all the areas to be excluded [labeled either blue or yellow in panel (b)]. The gray area represents snow with brighter gray scales corresponding to higher observed snow reflectance. Panel (d) is the snow albedo after anisotropic correction. The albedo scale for panels (c) and (d) is represented by the wedge on the right of panel (d). Panels e and f are similar to panels c and d but for channel 2. The observed isotropic albedos shown in panels c and e show a higher value on the left side of the image than the right side. The albedos after anisotropic correction (panels d and f), however, are quite uniform, which indicates that the actual snow albedo does not vary much over the entire image. The postlaunch calibration was not applied here because the objective was only to remove the angular variation of snow albedo.

To show the effectiveness of the anisotropic correction, Fig. 9 compares the histograms of TOA snow albedo before and after the anisotropic correction. Panels a and b in this figure are the histograms for channel 1 and correspond to panels c and d in Fig. 8, respectively. Panels c and d correspond to panels e and f in Fig. 8. Only the snow pixels in Fig. 8 are used in the histograms. Comparing the histograms before and after anisotropic correction, it is easy to see the more uniform nature of the albedo distributions after angular effects have been removed.
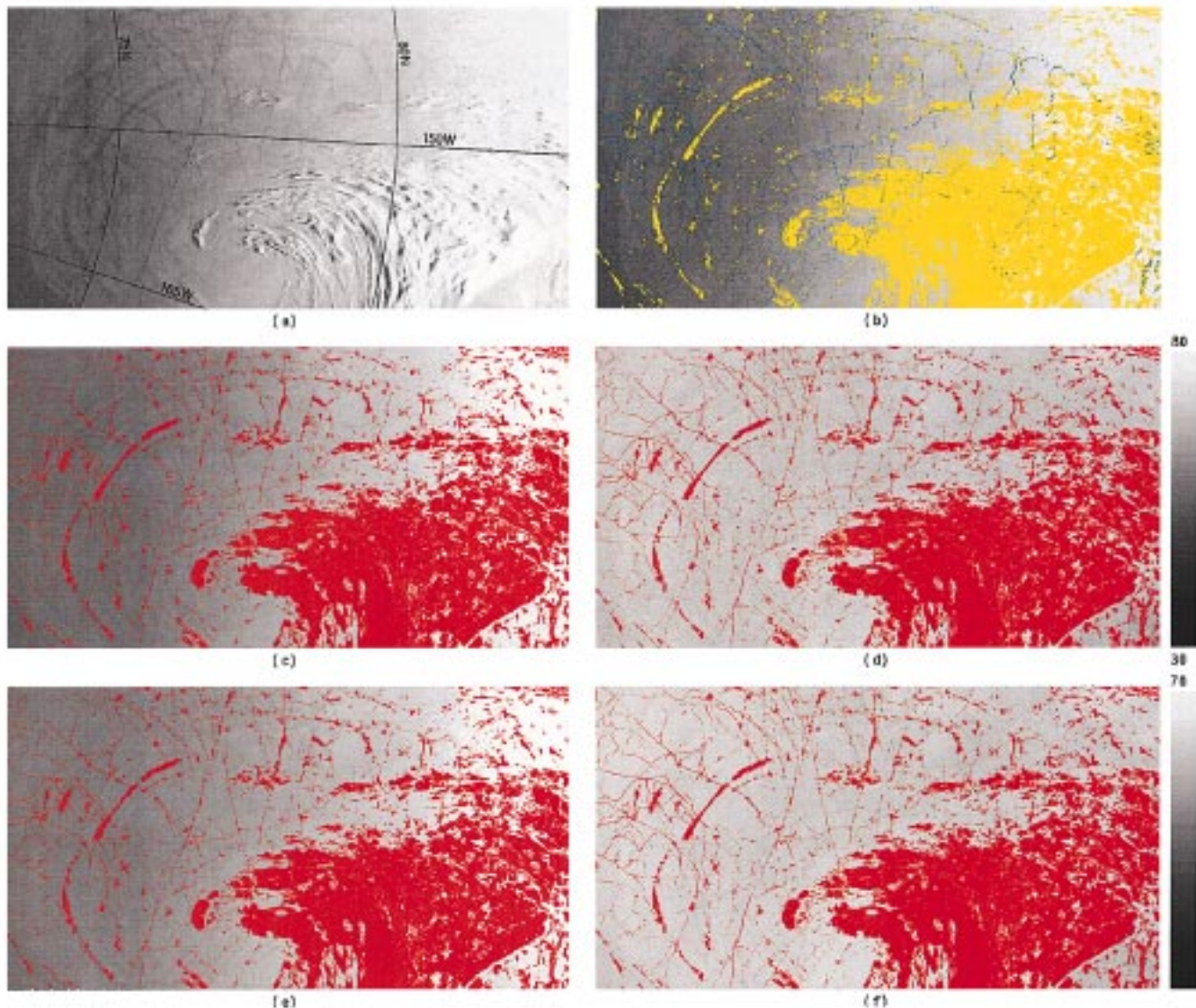
Fig. 12. Same as Fig. 8, but for an image taken over the Beaufort Sea on March 23, 1997.

The image in Fig. 10 was acquired over the northern Bering Strait between the Chuckchi Sea and the Beaufort Sea on March 26, 1997. The graphical presentation is similar to Fig. 8. The assigned clouds, labeled as yellow in panel (b), also included some snow pixels but are generally consistent with the cloud structure in panel (a). Leads are shown in blue. The satellite-observed isotropic albedos shown in panels c (channel 1) and e (channel 2) have higher values on the left side of the scene and lower ones on the right. The albedo after anisotropic correction (panels d and f) shows a lower albedo on the left and higher on the right, but their dynamic range is much smaller across the scene. Because the left side of the image is closer to the coast, the snow and atmospheric conditions may actually be different (e.g., higher pollution and more dust-contaminated snow) from those on the right side (which is closer to the inner Arctic). If this is the case, then the albedo pattern after correction might represent the actual albedo at the top of atmosphere better. Otherwise, the correction is somewhat overdone but still represents an improvement over the original data. Similar to Fig. 9, Fig. 11 compares the statistical albedo

distribution before and after anisotropic correction. Panels (a) and (b) correspond to panels (c) and (d) in Fig. 10 and panels (c) and (d) correspond to panels (e) and (f) in Fig. 10. This comparison also shows a much more spatially uniform albedo for the snow after the anisotropic correction.

Fig. 12 shows an image acquired over the Beaufort Sea on March 23, 1997. Its panels are analogous to those in Figs. 8 and 10. Fig. 13 is the histogram comparison for snow albedo before and after anisotropic correction for this image. Again, both panels (d) and (f) in Fig. 12 and the histogram for the albedo after correction [Fig. 13(b) and (d)] show that the albedo variation over the entire image due to the sun-satellite geometry is removed by the anisotropic correction.

Fig. 14 shows the relative difference of the isotropic albedo (α_{iso}) and the actual anisotropy-corrected albedo α for the three images shown and corrected above in this section. This difference (in %) is calculated as

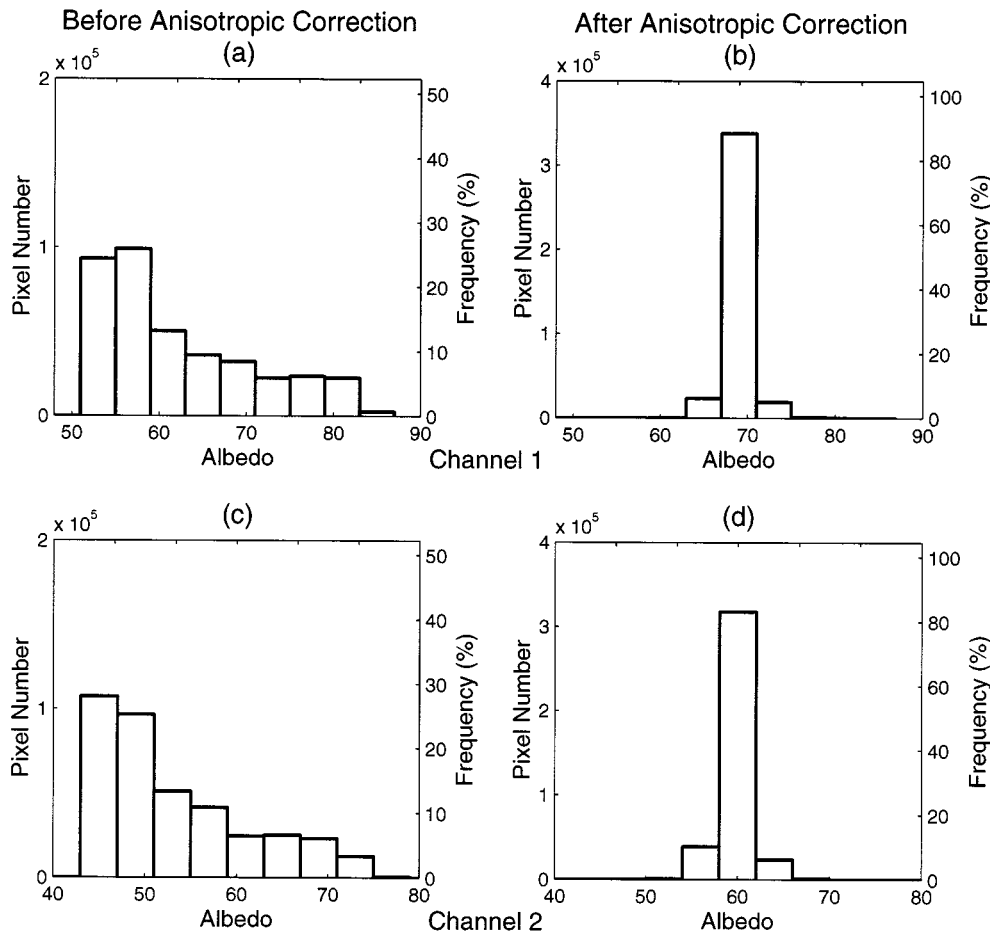$$DIF = \frac{\alpha_{iso} - \alpha}{\alpha} \times 100\% \qquad (7)$$

Fig. 13.   Same as Fig. 9, but for images in Fig. 12.

The relative difference is used because it is independent of any calibration error that might be large. The left panels are for channel 1 and the right panels are for channel 2. All results show that the isotropic albedo is higher than the actual albedo for large view angles in the forward-scattering direction (the left side of the images), and the difference increases as the view angle increases to the left of the image. The isotropic albedo, however, is lower than the actual value for small view angles (central portion of the images) and for backward-scattering directions (the right side of the images). For each image, the range of difference values is slightly larger in channel 2 than in channel 1, because there is a higher reflectance anisotropy of snow in channel 2.

The results in Fig. 14 indicate that the reflectance anisotropy could produce more than a ±20% relative error in the TOA snow albedo in both AVHRR channels 1 and 2. For pixels with larger satellite view angle, which were not included in the images presented, the error is expected to be even larger. According to any linear narrow-band to broad-band transformation, which has been widely used and formulated as (e.g., [11], [12], [35], [36])

$$\alpha = A\alpha_1 + B\alpha_2 + C \qquad (8)$$

a 20% error in AVHRR channel 1 albedo (α_1) and channel 2 albedo (α_2) means a same magnitude of error in the broad-band albedo for solar flux as A, B, and C are regression constants in

(8). This error in the TOA albedo, in turn, implies an approximate error of 70 Wm^{-2} of solar flux into or out of the atmosphere for a solar zenith angle of 70°. Considering the accuracy requirement of a few Wm^{-2} for climate modeling and the fact that the greenhouse effect of the CO_2 concentration doubling is only about an extra 4 Wm^{-2} radiation flux at the tropopause [37], this uncertainty is unacceptably large.

V. CONCLUSION

The viewing and illumination geometry (the solar, view, and relative azimuth angles) can introduce large artificial variations in images of snow reflectance acquired by the AVHRR instrument. This is contrary to the conclusion made in [38], based on observations from NIMBUS-7, that snow is the most nearly isotropic surface type. The nearly "isotropic" reflectance of snow was observed only in images obtained under certain view geometries (e.g., far away from the principal plane). The satellite-observed isotropic albedo is generally larger than the true albedo in the forward-scattering directions with large satellite view angle, whereas it is lower than the actual value for small view angles. The angular dependence of snow reflectance, which can greatly enlarge the variation of snow reflectance in some images, is so large that an anisotropic correction must be applied in conversion to albedo. The anisotropic features of the observed snow reflectance from AVHRR imagery are
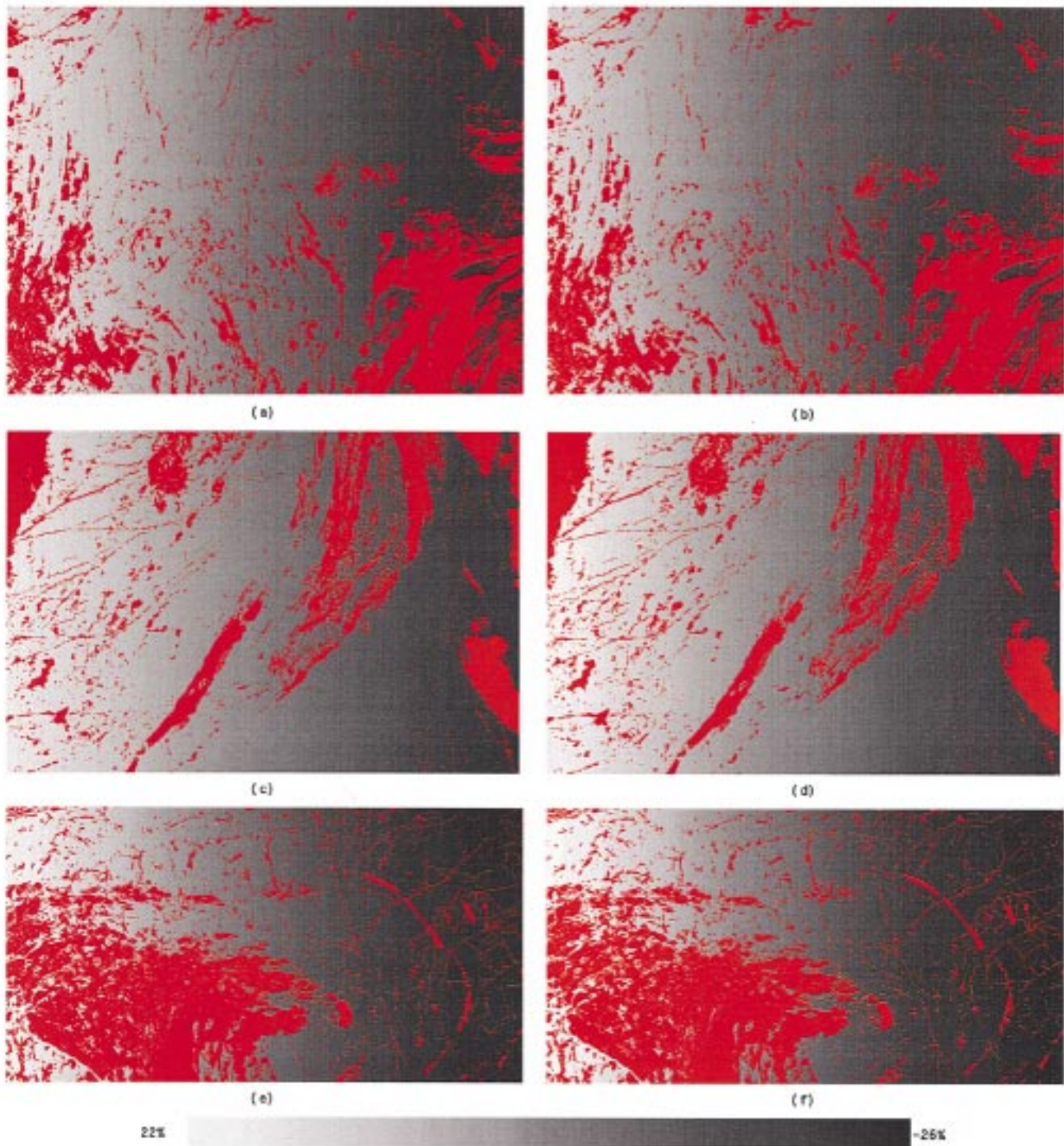
Fig. 14.   Relative difference between the satellite-observed isotropic albedo and the anisotropy-corrected albedo for snow in the three images presented in Figs. 8, 10 and 12. The red overlay represents the excluded pixels. The left panels are for AVHRR channel 1, and the right panels are for channel 2.

consistent with the theoretical analysis in Part I of this study [13]. Based on this theoretical study which was, in turn, based on the coupled radiative transfer model [17], [18], the observed anisotropic reflectance of snow can be well simulated and consequently, the anisotropy can be removed from the satellite-observed reflectance. A method for anisotropic correction was developed to remove the angular dependence over an entire image. Results show that this method is effective and efficient.

The snow reflectance variation becomes much smaller over images of snow on sea ice after the anisotropic correction algorithm is applied.

The images selected for study in this paper are limited to those obtained in the early Arctic spring. This was solely to simplify the parameterization of snow. The method for anisotropic correction developed herein, however, is general. For snow images acquired in other seasons, such as summer, the snow conditions

that are required for the correction algorithm would be more complicated and therefore, the physical parameters of snow for model input are more difficult to assume unless detailed *in situ* observation data to describe the snow/sea ice are available.

REFERENCES

[1] T. S. Ledley, "Snow on sea ice: Competing effects in shaping climate," *J. Geophys. Res.*, vol. 96, no. D9, pp. 17 195–17 208, Sept. 1991.

[2] J. A. Curry, J. L. Schramm, and E. E. Ebert, "On the ice albedo climate feedback over the Arctic ocean," *J. Climate*, vol. 8, pp. 240–247, 1995.

[3] J. E. Walsh, A. Lynch, and W. Chapman, "A regional model for studies of atmosphere-ice-ocean interaction in the Western Arctic," *Meteorol. Atmos. Phys.*, vol. 51, no. 3–4, pp. 179–194, 1993.

[4] R. A. De Abreu, D. G. Barber, K. Misurak, and E. F. LeDrew, "Spectral albedo of snow-covered first-year and multi-year sea ice during spring melt," *Ann. Glaciol.*, vol. 21, no. 1, pp. 337–342, 1995.

[5] D. K. Perovich, "Light reflection from sea ice during the onset of melt," *J. Geophys. Res.*, vol. 99, pp. 3351–3359, Feb. 1994.

[6] T. C. Grenfell, S. G. Warren, and P. C. Mullen, "Reflection of solar radiation by the Antarctic snow surface at ultraviolet, visible, and near-infrared wavelengths," *J. Geophys. Res.*, vol. 99, pp. 18669–18684, Sept. 1994.

[7] M. Haefliger, K. Steffen, and C. Fowler, "AVHRR surface temperature and narrow-band albedo comparison with ground measurements for the Greenland ice sheet," *Ann. Glaciol.*, vol. 17, no. 1, pp. 49–54, 1993.

[8] R. A. De Abreu, J. Key, J. A. Maslanik, M. C. Serreze, and E. F. LeDrew, "Comparison of *in situ* and AVHRR-derived broadband albedo over Arctic sea ice," *Arctic*, vol. 47, no. 3, pp. 288–297, 1994.

[9] A. J. Schweiger, M. C. Serreze, and J. R. Key, "Arctic sea ice albedo: A comparison of two satellite-derived data sets," *J. Geophys. Lett.*, vol. 20, no. 1, pp. 41–44, Jan. 1993.

[10] A. W. Nolin and J. C. Stroeve, "The changing albedo of the Greenland ice sheet: Implications for climate modeling," *Ann. Glaciol.*, vol. 25, pp. 51–57, 1997.

[11] J. C. Stroeve, A. W. Nolin, and K. Steffen, "Comparison of AVHRR-derived and *in situ* surface albedo over the Greenland ice sheet," *Remote. Sens. Environ.*, vol. 62, pp. 262–276, 1997.

[12] R. W. Lindsay and D. A. Rothrock, "Arctic sea ice albedo from AVHRR," *J. Climate*, vol. 7, no. 11, pp. 1737–1749, 1994.

[13] Z. Jin and J. J. Simpson, "Bidirectional anisotropic reflectance of snow and sea ice in AVHRR channel 1 and 2 spectral regions—Part I: Theoretical analysis," *IEEE Trans. Geosci. Remote Sensing*, vol. 37, pp. 543–554, Jan. 1999.

[14] K. B. Kidwell, *NOAA Polar Orbiter Data Users' Guide.* Washington, DC: NOAA, 1997.

[15] C. R. N. Rao and J. Chen, "Post-launch calibration of the visible and near-infrared channels of the Advanced very high resolution radiometer on the NOAA-14 spacecraft," *Int. J. Remote Sensing*, vol. 17, no. 14, pp. 2743–2747, 1996.

[16] J. F. Le Marshall, J. Simpson, and Z. Jin, "Satellite calibration using a collocated nadir observation technique: Theoretical basis and application to the GMS-5 pathfinder benchmark period," *IEEE Trans. Geosci. Remote Sensing*, vol. 37, pp. 499–507, Jan. 1999.

[17] Z. Jin, K. Stamnes, W. F. Weeks, and S. C. Tsay, "The effects of sea ice on the solar energy budget in the atmosphere-sea ice-ocean system: A model study," *J. Geophys. Res.*, vol. 99, pp. 25 281–25 294, Dec. 1994.

[18] Z. Jin and K. Stamnes, "Radiative transfer in non-uniformly refracting layered media: Atmosphere-ocean system," *Appl. Opt.*, vol. 33, pp. 431–442, Jan. 1994.

[19] C. Mobley, B. Gentili, H. Gordon, Z. Jin, G. Kattawar, A. Morel, P. Reinersman, K. Stamnes, and R. Stavn, "Comparison of numerical models for computing underwater light fields," *Appl. Opt.*, vol. 32, pp. 7484–7504, Dec. 1993.

[20] S. C. Tsay, K. Stamnes, and K. Jayaweera, "Radiative energy budget in the cloudy and hazy Arctic," *J. Atmos. Sci.*, vol. 46, no. 7, pp. 1002–1018, Apr. 1989.

[21] J. Zeng, R. McKenzie, K. Stamnes, M. Wineland, and J. Rosen, "Measured UV spectra compared with discrete ordinate method simulations," *J. Geophys. Res.*, vol. 99, no. D11, pp. 23019–23030, Nov. 1994.

[22] W. Han, K. Stamnes, and D. Lubin, "Remolte sensing of surface and cloud properties in the Arctic from AVHRR measurements," *J. Appl. Meteorol.*, in press.

[23] W. B. Tucker, A. J. Gow, and W. F. Weeks, "Physical propertie of summer sea ice in Fram Strait," *J. Geophys. Res.*, vol. 92, no. C7, pp. 6787–6803, 1987.

[24] G. A. Maykut and N. Untersteiner, "Some results from a time dependent thermodynamic model of sea ice," *J. Geophys. Res.*, vol. 76, no. 6, pp. 1550–1575, 1971.

[25] E. O. Lewis, C. E. Livingstone, C. Garrity, and J. R. Rossiter, "Properties of snow and ice," in *Remote Sensikng of Sea Ice and Icebergs.* New York: Wiley, 1994, ch. 2, pp. 21–96.

[26] W. B. Tucker, D. K. Perovich, A. J. Gow, W. F. Weeks, and M. R. Drinkwater, "Physical properties of sea ice relevant to remote sensing," in *Microwave Remote Sensing of Sea Ice.* Washington, DC: AGU, 1992, ch. 2, pp. 9–28.

[27] W. J. Wiscombe and S. G. Warren, "A model for the spectral albedos of snow, 1, Pure snow," *J. Atmos. Sci.*, vol. 37, pp. 2712–2733, Dec. 1980.

[28] D. G. Barber, S. P. Reddan, and E. F. LeDrew, "Statistical characterization of the geophysical and electrical properties of snow on landfast first-year sea ice," *J. Geophys. Res.*, vol. 100, pp. 2673–2686, Feb. 1995.

[29] S. G. Warren, R. E. Brandt, and P. O. Hinton, "Effect of surface roughness on bidirectional reflectance of Antarctic snow," *J. Geophys. Res.*, vol. 103, no. E11, pp. 25 789–25 807, Oct. 1998.

[30] M. Mishchenko, "Asymmetry parameters of the phase function for densely packed scattering grains," *J. Quant. Spectrosc. Radiat. Transf.*, vol. 52, no. 1, pp. 95–110, 1994.

[31] I. Dirmirhin and F. D. Eaton, "Some characteristics of the albedo of snow," *J. Appl. Meteorol.*, vol. 14, pp. 375–379, Apr. 1975.

[32] V. V. Salomonson and W. E. Marlatt, "Anisotropic solar reflectance over white sand, snow and stratus clouds," *J. Appl. Meteorol.*, vol. 7, pp. 475–483, June 1968.

[33] T. C. Grenfell, S. G. Warren, and P. C. Mullen, "Reflection of solar radiation by the Antarctic snow surface at ultraviolet, visible, and near-infrared wavelengths," *J. Geophys. Res.*, vol. 99, no. D9, pp. 18 669–18 684, Sept. 1994.

[34] A. K. Jain, *Fundamentals of Digital Image Processing.* Englewood Cliffs, NJ: Prentice-Hall, 1989, ch. 7, pp. 233–266.

[35] Z. Li and H. G. Leighton, "Narrowband to broadband conversion with spatially autocorrelated reflectance measurements," *J. Appl. Meteorol.*, vol. 31, pp. 421–432, May 1992.

[36] R. Hucek and H. Jacobowitz, "Impact of scene dependence on AVHRR albedo models," *J. Atmos. Ocean. Technol.*, vol. 12, pp. 697–711, Aug. 1995.

[37] J. T. Houghton, L. G. Meira Filho, B. A. Callander, N. Harris, A. Kattenberg, and K. Maskell, Eds., "IPCC," in *Climate Change 1995: The Science of Climate Change.* Cambridge, MA: Cambridge Univ. Press, 1996.

[38] V. R. Taylor and L. L. Stowe, "Reflectance characteristics of uniform earth and cloud surfaces derived from Nimbus-7 ERB," *J. Geophys. Res.*, vol. 89, pp. 4987–4996, June 1984.

Zhonghai Jin received the B.S. degree in space physics from the University of Science and Technology of China, in 1984, the M.S. degree in optics from the Anhui Institute of Optics and Fine Mechanics, Chinese Academy of Sciences, in 1987, and the Ph.D. degree in atmospheric sciences from the University of Alaska, Fairbanks, in 1995.

He developed a coupled radiative transfer model for the atmosphere, sea ice, and ocean system while with the University of Alaska. He is currently a Postgraduate Research Oceanographer with the Scripps Institute of Oceanography, University of California at San Diego, La Jolla, CA. His research interests include the radiative transfer and its applications to remote sensing and image processing.

James J. Simpson received the B.S. degree in physics from the College of the Holy Cross, Worcester, MA, in 1968, the M.S. degree in nuclear physics from the University of Notre Dame, IN, in 1970, and the Ph.D. degree in physical oceanography/air/sea interaction processes from Oregon State University, Corvallis, in 1976.

He has been with Scripps Institution of Oceanography, University of California at San Diego, La Jolla, since 1978. Since 1988, he has been Head and Principal Investigator of the Scripps Satellite Oceanography Center and the Digital Image Analysis Laboratory. His present research interests include geophysical imaging systems, image segmentations and classification, image algebras, physical/statistical-based algorithms for geophysical retrievals from satellite data, and the development of data management and distribution systems for large geophysical data sets.